Obtaining Meteorologically Significant Surface Divergence Fields Through the Filtering Property of Objective Analysis

CHARLES A. DOSWELL III

Techniques Development Unit, National Severe Storms Forecast Center, Kansas City, Mo. 64106

(Manuscript received 19 January 1977, in final form 18 March 1977)

ABSTRACT

A method is developed for designing specific filtering properties into a weighted-average interpolation scheme. Both spatial and temporal filtering are simultaneously accomplished, resulting in good time continuity as well as smooth spatial patterns. Both low-pass and band-pass filters are shown, with the band-pass results designed to emphasize details of the fields at the resolution limits for conventional surface data. These filters are applied to surface data on a severe thunderstorm day in Oklahoma. Results suggest that divergence fields calculated from the filtered data are well correlated with severe weather events, which develop only after several hours of preexisting moisture convergence.

1. Introduction

Owing to the high noise level, use of conventional surface observations has generally been limited to subjective analysis. Experienced human analysts have been able to use the high data density of the surface observations to reveal weather patterns on a scale well below that of the upper air network (Magor, 1958; House, 1964). An important feature of subjective analysis is the ability of the analyst to impose temporal continuity, which prevents any single observation from unduly affecting the analysis.

However, subjective analysis suffers from several limitations. The results are not reproducible, and it usually takes years of experience before an analyst attains a high level of expertise. Each analyst will treat a given situation differently and the differences can be particularly significant if forecasts are involved. Also, it is generally conceded that derived quantities, such as vorticity and divergence, can only be subjectively estimated from a subjective analysis.

One solution to this problem is to perform an "objective analysis", which usually means an interpolation of the irregularly spaced data to a regular mesh of grid points. This approach has been used by Charba (1975) and Hudson (1971), among others, to compute moisture divergence fields. As suggested by Charba's results and the operational applications shown by Ostby (1975), surface moisture convergence can be a good predictor for severe weather.

A significant problem still remains if this approach is taken. Experience with hourly computations of surface moisture divergence indicates that the patterns show relatively poor spatial and temporal continuity. This is a result of high-frequency, short-wavelength "noise" in the objectively interpolated fields of wind and moisture. Post-interpolation smoothing is one way to suppress spatial noise, but no solution is obtained for the excessive temporal variation. Presumably, a subsequent temporal smoothing could be used to force temporal continuity, but substantial computation time is required for such a smoothing approach. Another problem is that all objective interpolation techniques have filtering properties (Barnes, 1964; Stephens and Polan, 1971) which may not be compatible with post-interpolation filter functions.

2. Filter technique

An economical way to solve these problems has been developed by exploiting the inherent filtering properties of the interpolation scheme. This technique filters simultaneously in space and time, imposing a time continuity analogous to that of a subjective analyst. Owing to its simple functional form, the interpolation scheme of Barnes (1973) is used to develop the desired filtering characteristics. If R^* and T^* denote the dimensional space and time separation of a datum from a grid point and $\tilde{\phi}$ the observed value, then the value ϕ assigned to the grid point is simply the weighted average, given by

$$\phi=\sum_{m=1}^{M} w_m(R^*,T^*;\kappa,\eta)\tilde{\phi}_m/\sum_{m=1}^{M} w_m(R^*,T^*;\kappa,\eta). \quad (1)$$

There are M datum points within R_c^* and T_c^* from the grid point and the weight assigned to the mth datum is w_m, where

$$w_m(R^*,T^*;\kappa,\eta)=\exp(-R_m^{*2}/4\kappa-T_m^{*2}/4\eta). \quad (2)$$

The limiting values R_c^* and T_c^* depend, in part, on the

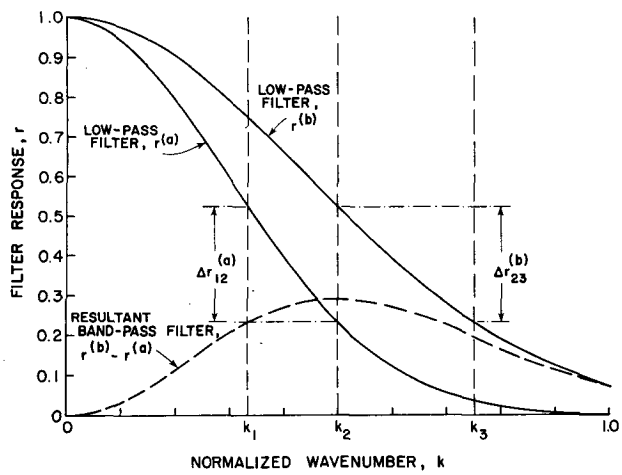

FIG. 1. Schematic illustration of band-pass filter design with the notation explained in the text.

choices of κ and η. The parameters κ and η are at our disposal for filter design; the limits on R^* and T^* are chosen so there is negligible contribution from data outside those limits. Barnes (1973) has shown that the response function in the spectral domain corresponding to (2) is

$$r(k^*,\nu^*;\kappa,\eta)=\exp(-\kappa k^{*2}-\eta\nu^{*2}), \tag{3}$$

where k^* and ν^* are the dimensional wavenumber and frequency. Observe that the theoretical response functions used in this study assume continuous variables in space and time, as well as in the spectral domain. In reality, the data and the grid are discrete, which implies that true response will depart from the theoretical, with the implication that this departure will increase as the wavelength and/or period decrease.

It is convenient to nondimensionalize in both the space-time and spectral domains, based on the grid lengths, so that the results can be applied to any grid. Any further reference to "length" or "wavenumber" in the text is now to include both space and time, but spatial and temporal notation are kept distinct. A convenient characteristic length is twice the grid length (the minimum resolvable wavelength). A wave of length $L^*=\lambda\Delta S$ (λ is not necessarily an integer) then has a nondimensional wavenumber given by

$$k=\frac{2\pi}{(\lambda\Delta S)}\frac{(2\Delta S)}{2\pi}=\frac{2}{\lambda}.$$

Similarly,

$$\nu=\frac{2\pi}{(\tau\Delta t)}\frac{(2\Delta t)}{2\pi}=\frac{2}{\tau}.$$

In the spatial domain, let a characteristic length be some arbitrary multiple (choose an integer for convenience) of the grid length, say $\rho\Delta S$. Then the nondimensional distance is

$$R=\frac{R^*}{\rho\Delta S} \quad \text{or} \quad \rho R=\frac{R^*}{\Delta S},$$

while the nondimensional time separation is

$$T=\frac{T^*}{\gamma\Delta t} \quad \text{or} \quad \gamma T=\frac{T^*}{\Delta t}.$$

Observe that the analysis parameters (κ and η) have dimensions of "length" squared. We define nondimensional parameters D and N such that

$$\kappa=D^2\Delta S^2, \quad \eta=N^2\Delta t^2.$$

Using this nondimensionalization (2) and (3) can be written as

$$w(R,T;D,N)=\exp[-(\rho R/2D)^2-(\gamma T/2N)^2], \tag{4}$$

$$r(k,\nu;D,N)=\exp[-(\pi Dk)^2-(\pi N\nu)^2]. \tag{5}$$

For simplicity, we consider the spatial domain alone. If $\Delta r_{ij}^{(m)}$ is the response difference, for a given $D=D_m$, between wavenumbers k_i and k_j, where $k_i<k_j$, i.e.,

$$\Delta r_{ij}^{(m)}=r(k_i;D_m)-r(k_j;D_m),$$

then a band-pass filter is obtained with peak response at $k=k_2$ if $\Delta r_{12}^{(a)}$ and $\Delta r_{23}^{(b)}$ are simultaneously maximized, subject to the constraint

$$\Delta r_{12}^{(a)}=\Delta r_{23}^{(b)}. \tag{6}$$

This process is illustrated schematically in Fig. 1. Maxima are obtained, with respect to the response parameters D_a and D_b, whenever

$$\left.\begin{aligned}\frac{\partial}{\partial D_a}[\Delta r_{12}^{(a)}]=0\\ \frac{\partial}{\partial D_b}[\Delta r_{23}^{(b)}]=0\end{aligned}\right\}. \tag{7}$$

Thus, in space, the band-pass filter centered at $k=k_2$ is found by solving the system

$$D_a^2=\frac{2\ln(k_1/k_2)}{\pi^2(k_1^2-k_2^2)}, \tag{8a}$$

$$D_b^2=\frac{2\ln(k_2/k_3)}{\pi^2(k_2^2-k_3^2)}, \tag{8b}$$

$$k_1=(1/\pi D_a)[-\ln\{\exp[-(\pi D_a k_2)^2]+\exp[-(\pi D_b k_2)^2]-\exp[-(\pi D_b k_3)^2]\}]^{\frac{1}{2}}. \tag{8c}$$

Having chosen k_2 and k_3, Eq. (8b) is solved for D_b; the constraint then requires iteration on D_a and k_1, until both (8a) and (8c) can be simultaneously satisfied. In

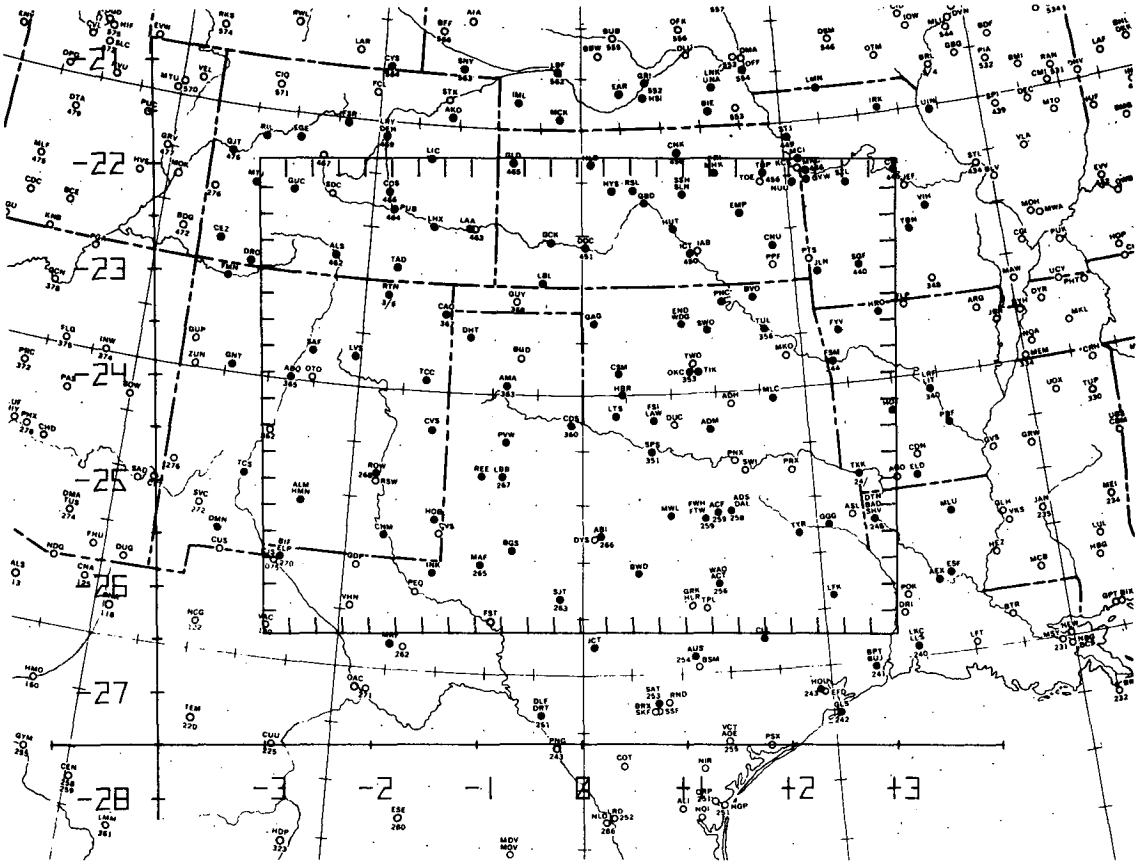

FIG. 2. Location of analysis grid and surface observation stations (dark circles) used for filtering; coordinates are shown in map inches on a polar sterographic projection, true at latitude 60°N with a scale of 1:10 million.

practice (8c) is not sensitive to D_a, so that the system converges rapidly to a solution for k_1 and D_a.

Band-pass filtering proceeds as follows: Data are interpolated to grid points using weight function

$$w(R,T;D_a,N_a)=\exp\left[-\frac{(\rho R)^2}{4D_a^2}-\frac{(\gamma T)^2}{4N_a^2}\right]$$

and again using weight function

$$w(R,T;D_b,N_b)=\exp\left[-\frac{(\rho R)^2}{4D_b^2}-\frac{(\gamma T)^2}{4N_b^2}\right]$$

which yield grid point values for the analyzed field of $\phi^{(a)}$ and $\phi^{(b)}$, respectively. Since the bands are centered at k_2 and ν_2 (in space and time), the difference in response at the band center is

$$\delta r=\exp\{-[(\pi D_b k_2)^2+(\pi N_b \nu_2)^2]\}-\exp\{-[(\pi D_a k_2)^2+(\pi N_a \nu_2)^2]\},$$

so that the response at the band center can be normalized to give a band-pass analyzed value of

$$\phi^{(b-a)}=(1/\delta r)[\phi^{(b)}-\phi^{(a)}].$$

Each of the two interpolations is a low-pass filter, the difference being exploited to give the desired band-pass characteristics. For purposes of this paper, a "low-pass" field is chosen to be $\phi^{(a)}$.

3. The case of 18 June 1973

In order to demonstrate the technique, a case study involving a local outbreak of severe weather is examined using conventional surface observations. However, before proceeding with the case study, it is necessary to discuss several aspects of the data and the analysis as they pertain to this application of filtering.

The spatial nature of the grid is depicted in Fig. 2. Analysis is performed at hourly intervals, beginning at 1200 (all times GMT) and ending at 0000 on the following day. The observations used in the analysis are extracted from the WBAN-10 (or equivalent) forms at the sites indicated on Fig. 2, and consist of altimeter setting, temperature, dew-point temperature, wind speed and wind direction. A prefiltering was performed to remove gross errors before interpolation/filtering. A data set typically contains about 1800 observations from 125 stations, beginning at 1115 and ending at 0045 the following day.

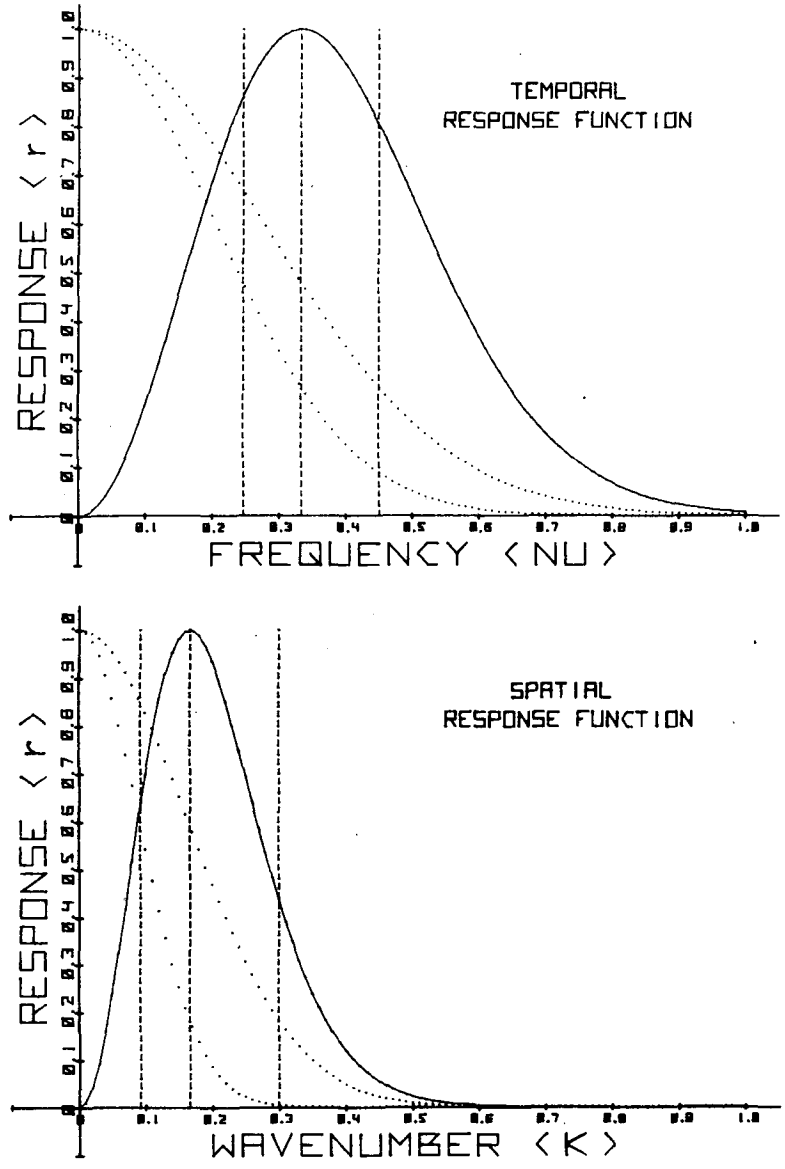

FIG. 3. Filter response curves for the low-pass and band-pass filters used. The solid curve is the band-pass filter, the lower dotted curve the low-pass filter. Both temporal and spatial curves are shown.

The analysis parameters used in this study are presented in Table 1. The response curves developed from this choice of parameters are shown in Fig. 3. Observe that the band centers are at about six times the average data spacing (the spatial data spacing is roughly twice the grid spacing). This choice reflects the fact that in order to compute reliable derivatives at a given wavelength, the wave must be sampled roughly six times (Phillips, 1973). Therefore, it is anticipated that quantities involving derivatives of the filtered data are reliable down to wavelengths sampled a sufficient number of times.

This brings up the issue of aliasing. Large amplitude waves on scales below the resolution limits of the data can, of course, seriously contaminate the analysis. This problem has always plagued users of surface data. An especially serious aspect of this problem is that it is not known into which wavelength the unresolved waves are folded, or to what extent. Naturally, this problem has not been totally resolved here. However, the time weighting used in this analysis should be able to eliminate much of the spatial aliasing, since the unresolved waves are not likely to be folded into longer wavelengths in a fashion which is temporally consistent. The inverse argument can be applied to the temporal aliasing. By filtering simultaneously in space *and* time, the result is likely to be improved with respect to the aliasing problem over either spatial or temporal filtering

TABLE 1. Analysis parameters.

Nondimensional wavenumber	Dimensional wavelength (km)
(k_1) 0.093	1.37×10^3
(k_2) 0.167	7.12×10^2
(k_3) 0.300	4.23×10^2
Nondimensional frequency	**Dimensional period (min)**
(ν_1) 0.247	4.86×10^2
(ν_2) 0.333	3.60×10^2
(ν_3) 0.450	2.67×10^2
Spatial analysis parameter (nondimensional)	**Dimensional equivalent (km²)**
(D_a) 1.384	$4\kappa=7.72\times10^3$
(D_b) 2.490	$4\kappa=2.50\times10^4$
Temporal analysis parameter (nondimensional)	**Dimensional equivalent (min²)**
(N_a) 0.665	$4\eta=2.94\times10^2$
(N_b) 1.213	$4\eta=4.36\times10^2$

Spatial grid interval: $\Delta s=0.25$ inch (on map) ≈ 63.5 km
Temporal grid interval: $\Delta t=60$ min

done separately. This is not to assert that aliasing is not present in the filtered fields, but to suggest that the technique presented here has potential for improving the situation. With this in mind, consider the case study presented here.

The synoptic pattern of 18 June 1973 is typical of local, late spring outbreaks of severe weather in Oklahoma. The 1200 GMT 500 mb analysis (Fig. 4) shows relatively weak flow (about 10 m s^{-1}) over Oklahoma, with little apparent prospect for strengthening during the day. The conventional surface analysis at 1200 (Fig. 5) depicts a cold front entering Oklahoma from the northwest. Conventional analysis, as is typical, does not include a dryline. Examination of the 1200 sounding at Tinker AFB (Fig. 7) shows potentially and

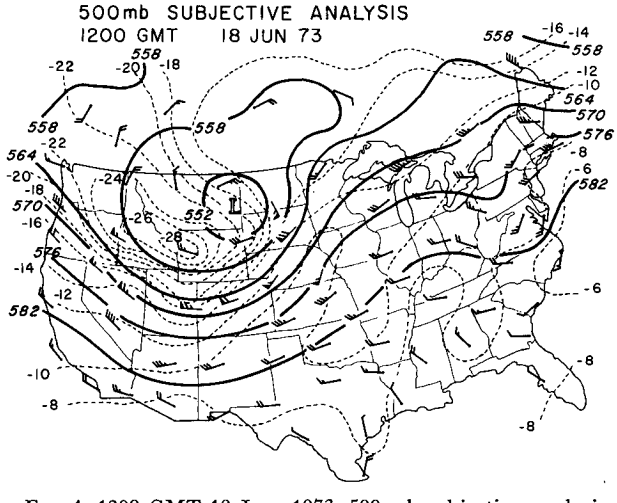

FIG. 4. 1200 GMT 18 June 1973, 500 mb subjective analysis. Solid lines are height contours (dam); dashed lines are isotherms (°C).

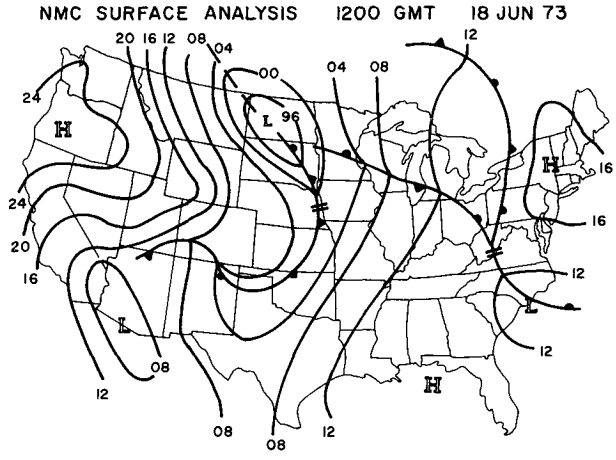

FIG. 5. 1200 GMT 18 June 1973, NMC surface analysis with sea level isobars (mb) and conventional notation.

convectively unstable stratification, with substantial lifting and/or low-level heating necessary to realize the instability. Maximum winds aloft reach about 25–30 m s^{-1} in the vicinity of 200 mb.

By 1800 GMT, the conventional surface analysis (Fig. 6) suggests that the front has slowed considerably, with a closed low-pressure center depicted in the southern Texas Panhandle. An ATS-3 satellite photograph (Fig. 8) taken at 1821 GMT shows a line of towering cumulus, which terminates in southwestern Oklahoma along the front. No cumulus is visible along the dryline, although small, poorly developed cumulus may, in fact, be present.

The low-pass filtered fields at 1800 (Fig. 9) confirm the conventional analysis and are, in turn, substantiated by it. The "low-pass" filter, as mentioned previously, is that with the lesser response of the two used in developing the band-pass filter. By performing the objective analysis, it is possible to determine readily such quantities as vorticity and moisture divergence on the large scale. Note that divergence, moisture

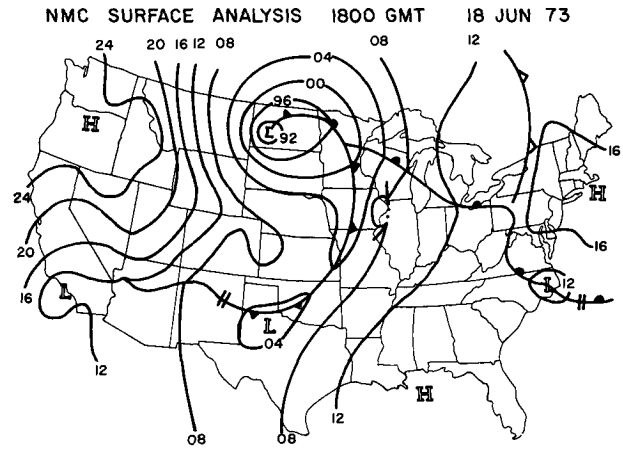

FIG. 6. As in Fig. 5 except for 1800 GMT.

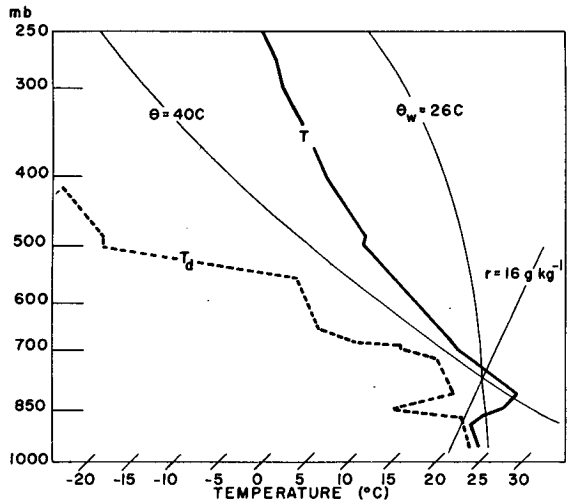

FIG. 7. Skew T, log p plot of 1200 GMT Tinker AFB rawinsonde. The temperature profile is the heavy solid line labeled T. The dew-point temperature profile is the heavy dashed line labeled T_d. The light solid lines are included for reference and show the 40°C potential temperature, the 26°C wet-bulb potential temperature, and the 16 g kg^{-1} mixing ratio curves. Wind profile follows conventional notation.

divergence and vorticity have been calculated via difference formulas that account for the variation of the map scale factor over the grid. It was observed that the large-scale patterns, as depicted by the low-pass filter, changed relatively slowly during the day of 18 June 1973. The changes reflect the southeastward progression of the front across Oklahoma and the normal diurnal trends.

Concurrent band-pass fields at 1800 (Fig. 10) reveal a significant cyclonic circulation center (at the intersection of the front and the dryline) that has drifted slowly southeastward from a 1200 position in the Texas Panhandle to an 1800 location in southwestern Oklahoma. The strongest moisture convergence at 1200 was just northeast of this circulation, in agreement with

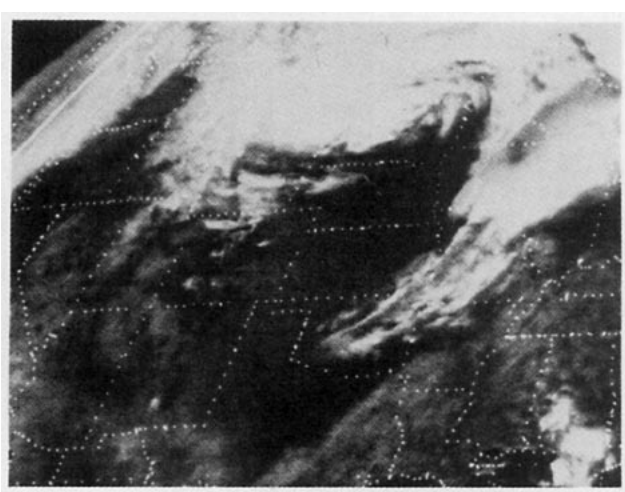

FIG. 8. Satellite photo taken at 1821 GMT.

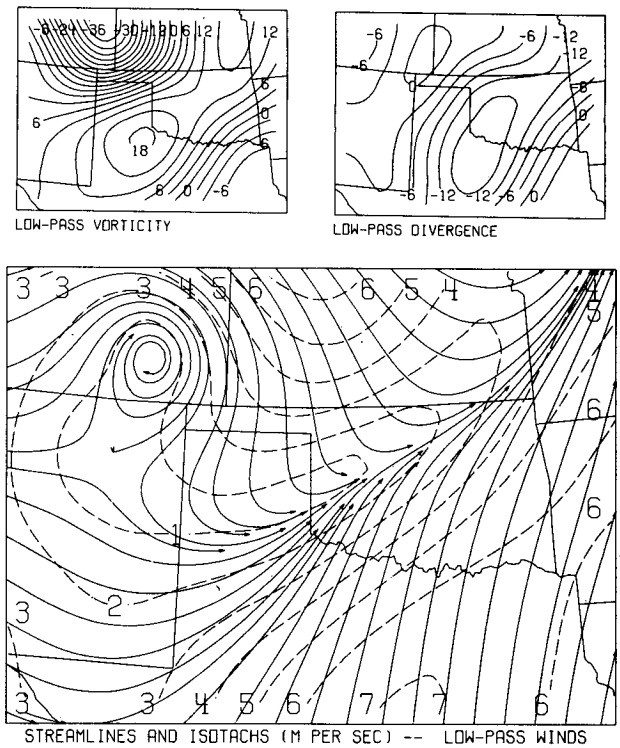

FIG. 9a. Low-pass filtered analysis of 18 June 1973 surface data at 1800 GMT, showing surface flow, vorticity and divergence. Vorticity and divergence have units of $10^{-6}s^{-1}$.

Siebers *et al.* (1975). By 1800, the maximum moisture convergence is shifting southward to the dryline in Texas, south of the Red River. Observe that maximum kinematic convergence is somewhat west of the dryline, whereas the maximum moisture convergence is along the dryline. It was observed in the band-pass analysis that the shift of maximum moisture convergence south-

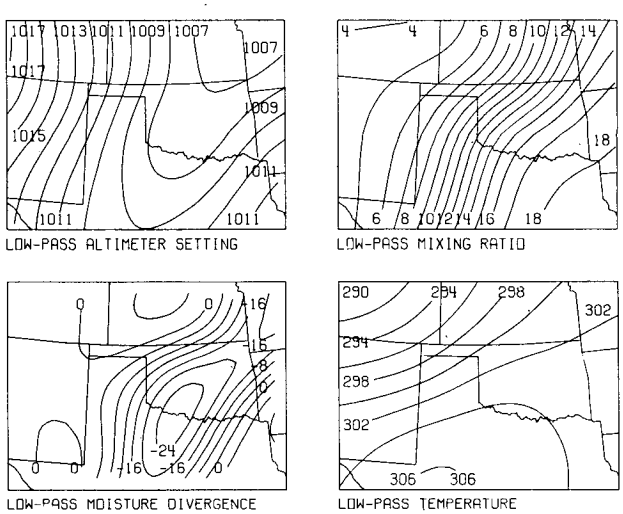

FIG. 9b. As in Fig. 9a showing 1800 GMT altimeter setting (mb), mixing ratio (g kg^{-1}), moisture divergence (10^{-5} g kg^{-1} s^{-1}) and temperature (K).

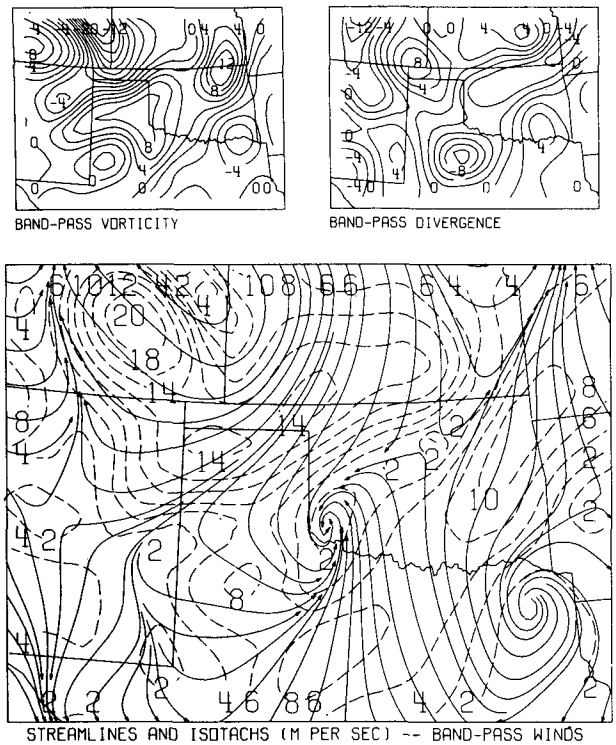

FIG. 10a. As in Fig. 9a except for band-pass filtered analysis. Vorticity and divergence have units of 10^{-5} s^{-1}.

ward to the dryline was accompanied by a substantial warming and drying west of the dryline, suggesting that west of the dryline, diurnal heating has strongly coupled the surface to higher levels in the troposphere. This is substantiated by increased wind speeds at 1800 in the dry air. These results are in agreement with Schaefer's (1974) study of the quiescent dryline.

The band-pass data provide considerably more detail than low-pass fields, including fronts and the dryline. That this objective analysis can, in fact, provide spatially and temporally continuous depiction of subsynoptic features is a measure of the success of the analysis. Perhaps the most convincing demonstration of the meteorological significance of the band-pass moisture convergence field is the ATS-3 photograph taken at 2242 GMT (Fig. 11) which shows three separate thunderstorm complexes, each located in one of the three distinct moisture convergence maxima of Fig. 10. Fig. 12 suggests that the band-pass filtered moisture convergence provides somewhat better spatial resolution in depicting the occurrence of tornadoes than does the low-pass analysis. Although it is not presented here, the sequence of hourly moisture divergence analyses from the band-pass filtered data shows clearly the temporal evolution of the three thunderstorm complexes in Oklahoma and Texas seen in Fig. 11. Corresponding, hourly low-pass moisture divergence fields

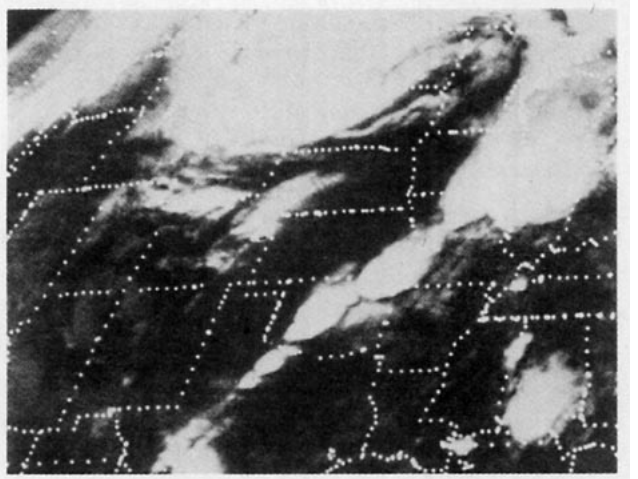

FIG. 11. Satellite photo taken at 2242 GMT.

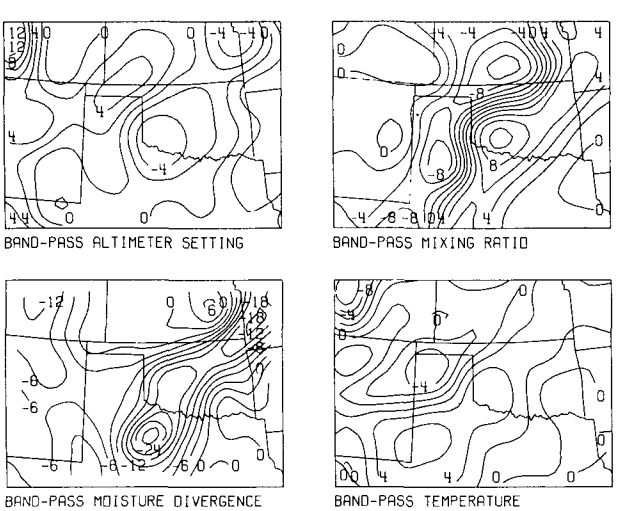

FIG. 10b. As in Fig. 9b except for band-pass filtered analysis. Moisture divergence has units of 10^{-4} g kg^{-1} s^{-1}.

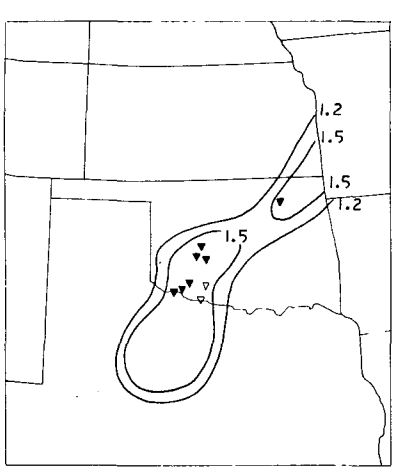

FIG. 12. Tornado reports, shown by solid triangles; funnel cloud reports, shown by open triangles; and moisture convergence isopleths adapted from Fig. 10b. All reports occurred after 1800 GMT.

(also not shown), in addition to lower spatial resolution, do not depict the temporal changes as clearly, but simply show a slow southward shift of maximum moisture convergence during the afternoon.

4. Discussion

As suggested by Siebers *et al.* (1975), the area to the northeast of a frontal wave is a well-documented area of high tornado potential. That this area is also clearly a band-pass moisture convergence maximum may shed some insights into the dynamics of "subsynoptic" systems (Doswell, 1976). That the moisture convergence precedes the development of thunderstorms by several hours indicates some potential for severe thunderstorm forecasting may be available in this analysis.

Clearly, unanswered questions remain, such as the lack of reported severe weather with storms that developed along the dryline. It is hoped that more case studies will be able to take advantage of this analysis tool to obtain quantitative information about low-level dynamics of the weather systems that produce severe weather. Upper air data will be difficult to incorporate, owing to the dramatic loss in resolution that occurs just off the surface. Questions about the timeliness and utility of the band-pass filtered analysis in an operational environment also remain.

Nevertheless, these results are encouraging. The technique can develop temporal continuity of analysis in a straightforward fashion. The analyzed fields can be space- and time-differentiated to provide usable derived fields like divergence without additional filtering, either before or after differentiation. Moisture divergence obtained in this manner is quantitatively compatible with physical intuition and, to a large extent, with observed meteorological events.

Other aspects of band-pass filtered fields are encouraging. In addition to the divergence calculations, the depiction of the dryline and frontal details is satisfactorily continuous and compatible with the efforts of skilled subjective analysts (e.g., Siebers *et al.*, 1975). Since divergence fields are treated in a satisfactory manner, it is likely that other kinematic properties of the flow such as vorticity and thermodynamic quantities like mixing ratio have been handled properly. By filtering the surface data in this controlled way, it is possible that more quantitative use can be made of the surface observations. It may now be feasible to integrate routinely such high resolution data into a more detailed depiction of the four-dimensional state of the atmosphere.

Acknowledgments. The author wishes to express his appreciation to Dr. Yoshi K. Sasaki of the University of Oklahoma, under whose guidance this research was carried out, to Drs. Edwin Kessler and Ronnie Alberty of the National Severe Storms Laboratory (NSSL) for very helpful discussions, and to my colleague, Dr. Joseph T. Schaefer of the Techniques Development Unit (TDU), for his unflagging assistance. This work was partially supported under National Science Foundation Grant GA 30976.

Also, the author thanks the NSSL computer processing section, headed by Ms. Kathyrn Gray, for many hours of sincerely appreciated effort, as well as the drafting of Ms. Jennifer Farris of NSSL and the typing and drafting of Ms. Deborah Barbieri of TDU.

REFERENCES

Barnes, S. L. 1964: A technique for maximizing details in numerical weather map analysis. *J. Appl. Meteor.*, **3**, 396–409.

——, 1973: Mesoscale objective map analysis using weighted time-series observations. NOAA Tech. Memo. ERLTM-NSSL-62, 60 pp. [NTIS Accession No. COM-73-10781].

Charba, J. P., 1975: Operational scheme for short-range forecasts of severe local weather. *Preprints Ninth Conf. Severe Local Storms*, Norman, Okla., Amer. Meteor. Soc., 51–57.

Doswell, C. A., III, 1976: Subsynoptic-scale dynamics as revealed by use of filtered surface data. NOAA Tech. Memo. ERLTM-NSSL-79, 40 pp. [NTIS Accession No. PB 265-433/AS].

House, D. C., 1964: The problem of detecting mesoscale motion systems. *Mon. Wea. Rev.*, **92**, 589–592.

Hudson, H. R., 1971: On the relationship between horizontal moisture convergence and convective cloud formation. *J. Appl. Meteor.*, **10**, 755–762.

Magor, B. W., 1958: A meso-low associated with a severe storm. *Mon. Wea. Rev.*, **86**, 81–90.

Ostby, F. P., 1975: An application of severe storm forecast techniques to the outbreak of June 8, 1974. *Preprints Ninth Conf. Severe Local Storms*, Norman, Okla., Amer. Meteor. Soc., 7–12.

Phillips, N. A., 1973: Principles of large scale numerical weather prediction. *Dynamic Meteorology*, P. Morel, Ed., D. Reidel, 3–95.

Schaefer, J. T., 1974: The life cycle of the dryline. *J. Appl. Meteor.*, **13**, 444–449.

Siebers, J. O., F. Hidalgo, S. A. Tegtmeier and M. Young, 1975: Guide for using GOES/SMS imagery in severe weather forecasting. Unnumbered technical guide from USAFETAC, Andrews AFB, Md., 56 pp.

Stephens, J. J., and A. L. Polan, 1971: Spectral modification by objective analysis. *Mon. Wea. Rev.*, **99**, 374–378.